

Properties of nanoscale copper oxide thin film deposited by plasma focus device

Hasan Anousha *

Abstract

In this study a 2 kJ Mather type plasma focus device was employed to deposit copper oxide (CuO) nanoscale thin film at room temperature on the glass substrate. The anode of the device was made of copper alloys. A mixture of oxygen and argon (O_2+Ar) gases was used as the working gas for CuO deposition. CuO nanostructures were formed on the glass substrate by 25 shots at 9 cm above the anode and 0° angle with respect to the anode axis. According to the XRD results, the crystallite size of the CuO thin film is between 64 and 122 nm. FESEM images show that the growth nanostructures on the surface of the film are almost clusters with the average size of 80 nm. UV-Vis spectroscopy results indicate that the transmittance of the deposited CuO thin films in the UV region is very low. The bandgap energy and refraction index of the film are 1.8 eV and 1.9, respectively. The $I-V$ diagram shows that as the applied voltage increases, the current intensity increases exponentially. Four-probe method shows that the electrical surface resistance of CuO thin film is in the range of $680 \Omega\text{cm}$, and their dc conductivity is about 13.2 S/m .

Keywords

Nanocoating, Plasma focus, Field emission scanning electron microscope, UV-Visible spectroscopy, I-V curve.

Department of Physics, Faculty of Basic Sciences, Azarbaijan Shahid Madani University, Tabriz, Iran

*Corresponding author: h.anousha@azaruniv.ac.ir

1. Introduction

Recently, nanostructured transition metal oxides (TMO) have gained great interest from the scientific community due to their different properties compared with corresponding bulk counterparts, which in turn provides promising applications in the various fields of technology [1]. CuO, categorized as a TMO, is a p-type, narrow-bandgap semiconductor. Copper Oxide has two common forms; cupric oxide (CuO), with a bandgap in the range of 1.2-2.1 eV and cuprous oxide (Cu_2O), with a bandgap of 2.1-2.6 eV [2]. In CuO the lattice structure has monoclinic symmetry, whereas Cu_2O has a cubic structure [3]. The CuO and Cu_2O thin films are widely used in several device applications such as thin film transistors, intelligent windows, IR detectors, optical limiters etc. [4-8]. CuO is attractive as a selective solar absorber since it has potential application in CuO-based homojunction or heterojunction solar cells due to its high optical absorption edge that matches the AM 1.5 solar spectrum [9, 10]. The optical bandgap of CuO obtained by reflectance spectroscopy studies shows that the synthesized CuO nanoparticles are good photo-catalysts for phenol degradation in the visible wavelength range [11]. A number of reports have been made on CuO thin films preparation by various techniques including magnetron sputtering, spray pyrolysis, microwave, sol-gel, chemical vapour deposition, pulsed laser deposition and vacuum thermal evaporation [1, 2, 12-21]. Fan et al. showed that the deposition rate, phase structures, optical, and electrical

properties of copper oxide films using reactive sputtering depended on the sputtering power and the oxygen flow rate. The films formed were polycrystalline with no obvious preference in crystal orientations, and all p-type CuO thin films showed an indirect optical gap of about 1.5 eV [12]. H. Saad et al. deposited CuO thin films on glass substrates by spray pyrolysis technique [15]. A. Sameer et al. deposited CuO thin films of different thicknesses on glass substrates by vacuum thermal evaporation [21]. In this study, the plasma focus device (PF) was employed to grow CuO film on the glass substrate. This is the first study that concerns the spectroscopy of CuO plasma focus thin film. Physical properties of plasmas, energetic ions, and electrons, as produced in PF discharges, are substantially different from the conventional plasma devices used for plasma nanofabrication. In particular, PF discharges provide new and unique opportunities in the processing and synthesis of new materials. Since PF discharges have a concise duration and produce plasmas of high ion density, the anode is exposed to a high energy density causing its pulverization and generating a vapor of material that allows a fast deposit. The synthesized sample were examined in their structure by XRD, in topography surface by FESEM and AFM, optical properties by UV-Vis, and electrical properties with I-V measurements.

The dense plasma focus (DPF) is a simple, cost-effective, and pulsed coaxial plasma accelerator utilizing a self-generated magnetic field to compress the plasma to high densities (10^{25} – 10^{26} m^{-3}) as well as high temperatures (1–2 keV) for a short time (7-10 s) [22]. The DPF is a promising source of hard/soft

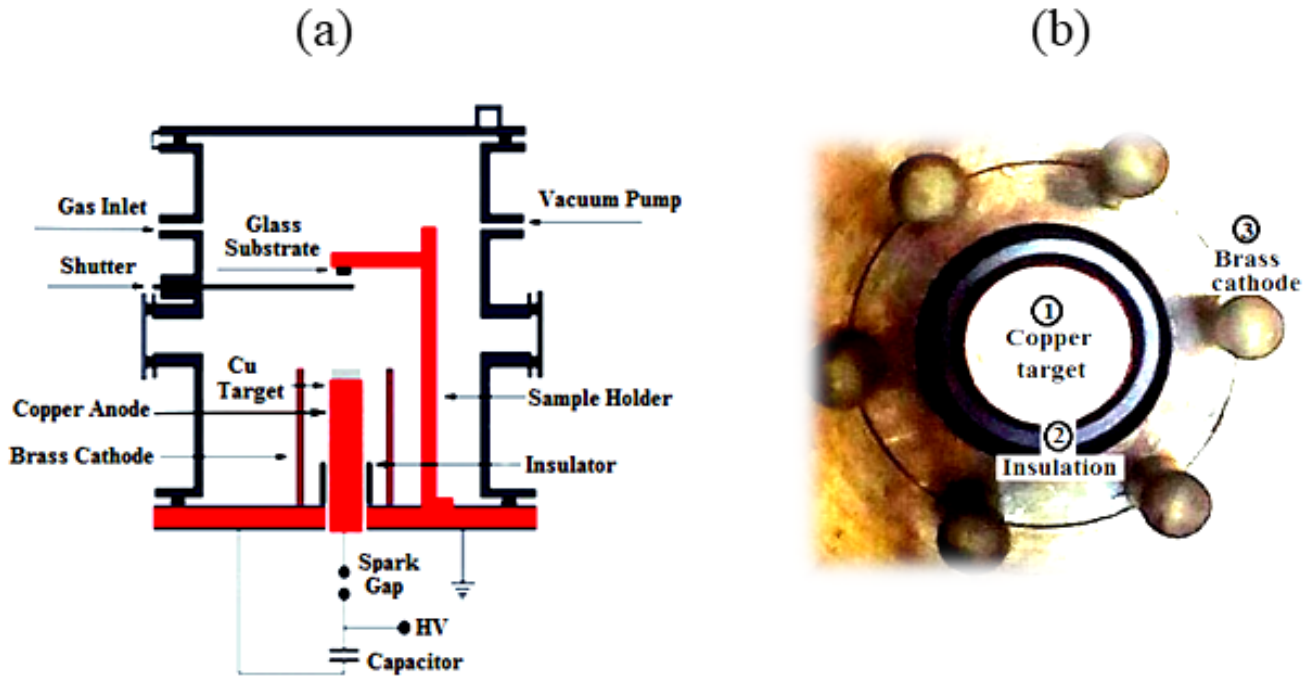


Figure 1. Schematic of Mather Plasma Focus Device (a) and inside on it (b).

X-rays, neutrons, relativistic electrons, and high energy ion beams over a broad energy spectrum [23]. While being primarily designed for fusion research applications, the DPF device has been recently considered for many purposes, including ion implantation, surface modification, thermal surface treatments, and thin film deposition [23–27].

2. Experimental Section

The used DPF device was Mather type having a 39 μF capacitor bank with the ability to be further charged up to 10

kV. The device consisted of a copper anode electrode with 1.8 cm of diameter and 5.3 cm of length, surrounded by six brass cathode electrodes, each with 5.3 cm of length. A Pyrex insulator has separated the electrodes (Fig 1).

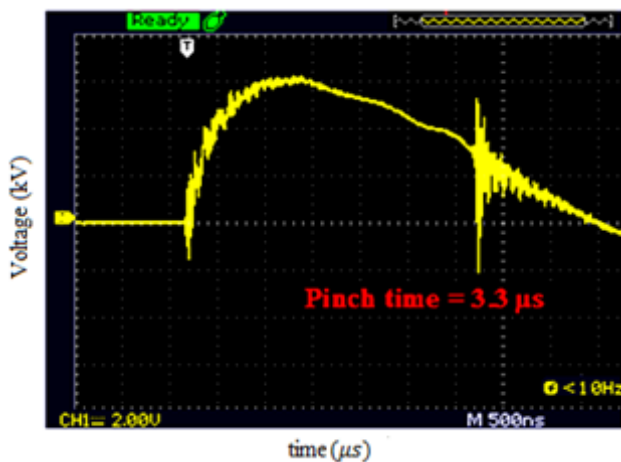


Figure 2. Rogowski coil current derivative signal at pinch time.

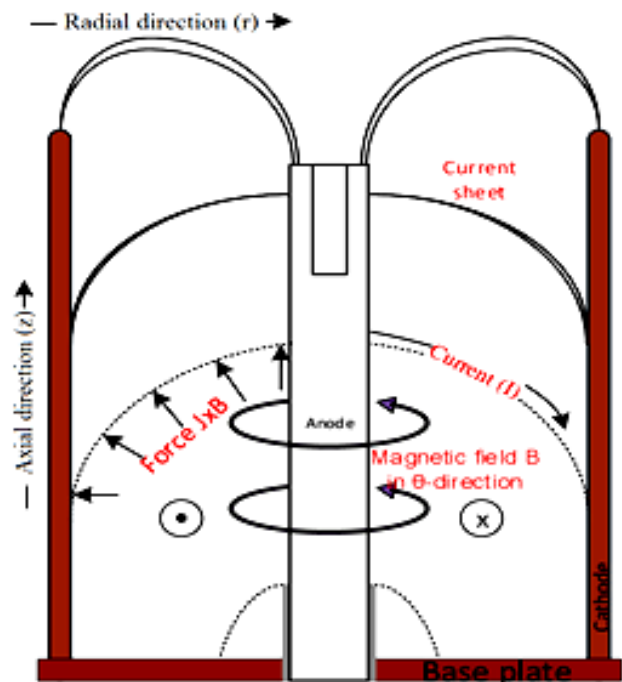


Figure 3. Performance of plasma focus device.

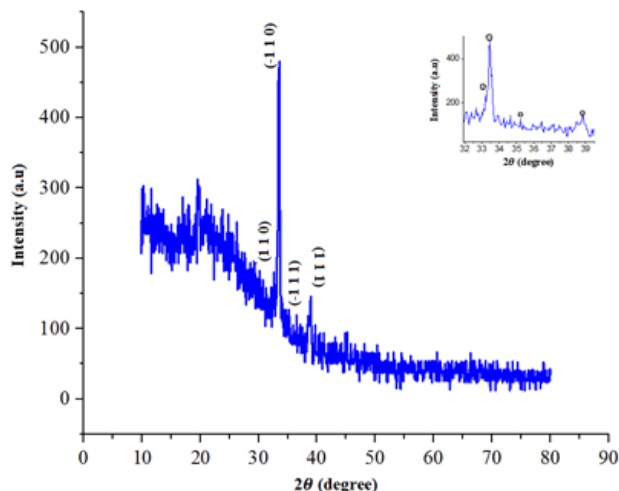


Figure 4. X-ray diffraction pattern of the CuO thin film.

In this experiment, the anode was made of the metal Cu (99.9% purity). There was a shutter between the anode electrode and the sample holder for the initial shots to achieve an excellent pinch. The entire set of electrodes was inside a vacuum container pressure-dropped by a rotary compressor to 0.2 Torr. Then, a mix of O₂ and Ar gases was injected inside the vacuum container as the working gas. The optimum pressure for the excellent pinch in the experiment was 0.2 Torr at 8.7 kV of voltage. The voltage waveform versus current at pinch time, which was received from the Rogowski coil, was recorded by an oscilloscope (Fig 2).

For the operation of the plasma focus device, a high voltage was applied between two anode and cathode electrodes by one 39 μF capacitor charged by a high voltage. Then, an electrical discharge took place on the insulator surface in 100 ns, creating a current layer on the insulator surface. A self-consistent magnetic field is created, producing Lorentz force and accelerating the current layer to the open end of the anode. As a result, the $\mathbf{J} \times \mathbf{B}$ force compressed the current layer on the anode, which created warm dense plasma. At this time, the plasma column created by the sausage instability ($m=0$) was eliminated by producing a high-energy electron, ion, and X-ray particles. Since a strong magnetic field created when the plasma column was eliminated, this magnetic field accel-

Table 1. The deposition conditions of the prepared copper oxide film.

Ar/O ₂ pressure ratio	1
Substrate	Glass
Target	Copper
Optimal voltage	8.7 kV
Number of shots	25
Distance	9 cm
Substrate temperature	RT

erated the ions and electrons in opposite directions such that the high-energy electrons collided with the anode (Cu) and resulted in their melt. Cu atoms were mixed with the ionized O₂ gas and deposited on the substrate at the pinching time by the produced plasma jet (Fig 3). Before the formation of the thin film, glass samples were cleaned with alcohol, acetone, and distilled water, each for 20 minutes in an ultrasonic device with the help of ultrasonic waves. The sample was placed 9 cm above the anode. CuO layer was also placed at 0° to the anode axis with 25 shots, being analyzed by XRD, FESEM, AFM, UV-Vis, and I-V chart.

The X-ray diffractometer (XRD) (PHILIPS PW1730) with Cu-K_α radiation of wavelength 1.5406 Å at a generator setting of 30 mA and 40 kV in the 2θ range from 10 to 80 degree and step size 0.05 degree was used to obtain the crystalline structure of the CuO thin film. The surface morphology of the film was analyzed by Field Emission Scanning Electron Microscopy (FESEM) (MIRA 3 TESCAN). Surface roughness was pictured and measured by an Atomic Force Microscope (AFM) (Ara Model No.0101/A). The UV-Visible-NIR spectrophotometer (Perkin Elmer-Lambda25) was employed to observe the optical properties of deposited film in the wavelength range from 200 to 1100 nm. The *I-V* measurements of CuO thin film was prepared for 2 Molar KOH solution and applied voltages from -0.5 to 1.5V and 20 mv/s rate.

3. Results and discussion

3.1 Structural properties

(1) X-ray Diffraction (XRD)

The XRD spectroscopy of the sample was done using the grazing technique, which is specific to thin layers and coatings. Figure 4 presents the X-ray diffraction pattern of the synthesized sample. From the XRD pattern of the sample exhibits diffraction peaks at 2θ equal to 32.60°, 33.40°, 35.20°, 38.80°. Based on the JCPDS card No. 01-089-5898 for CuO, the high peak at 33.40° is attributed to (-1 1 0) plane. The other three peaks at 32.60°, 35.20°, and 38.80° show the pref-

Table 2. Structural parameters of CuO thin film extracted from XRD diffraction pattern.

2θ(°)	32.6	33.4	35.2	38.8
(hkl)	(110)	(-110)	(-111)	(111)
d-Spacing (AA)	2.739	2.675	2.540	2.315
FWHM (°)	0.171	0.309	0.114	0.174
β (Rad)	0.003	0.0054	0.002	0.005
a (AA)	3.846	3.745	4.318	3.935
Crystallite size (nm)	122.6	64.1	86.6	100.5
Micro strain (%)	0.28	0.54	0.4	0.56
Crystal dislocation (×10 ⁻⁴ nm ⁻²)	0.6	2.4	1.3	0.9

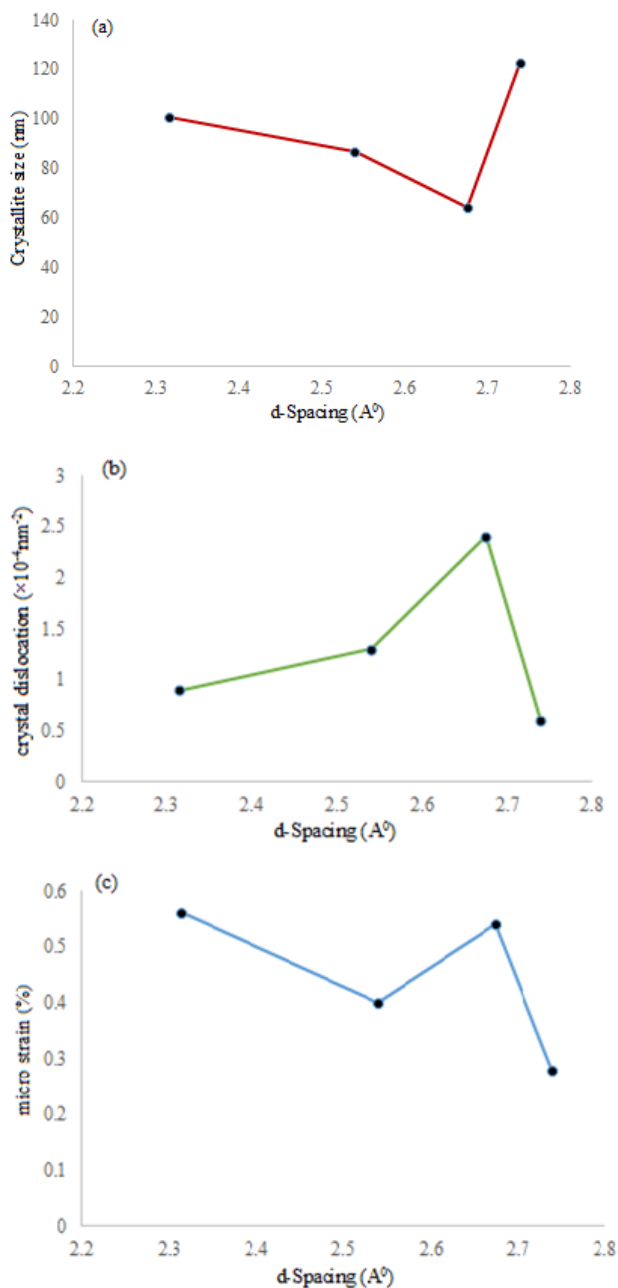


Figure 5. Chart of d-spacing variations in terms of (a) crystallite size, (b) crystal dislocation, and (c) a crystal microstrain.

erential orientations of (1 1 0), (-1 1 1), (1 1 1) copper oxide planes. Similar results were found by other authors [14, 15]. According to the XRD spectrum data, it can be concluded that the synthesized CuO thin film has a single-phase monoclinic structure. The following equations (1), (2), and (3) were used to extract the average sizes of the crystallites (D), crystal dislocation (δ), and micro strain of crystalline structure (ϵ) from

the width and angle of XRD peaks [28, 29];

$$D = \frac{k\lambda}{\beta \cos \theta} \quad (1)$$

$$\delta = \frac{1}{D^2} \quad (2)$$

$$\epsilon = \frac{\beta \cos \theta}{4} \quad (3)$$

where k is the shape factor ($k=0.94$), λ is the wavelength of the applied X-ray ($\lambda(\text{CuK}\alpha)=0.154056 \text{ nm}$), θ is the Bragg's angle, and β is the pure diffraction line broadening (in radians), which can be easily found by measuring the full width at the half maximum (FWHM). Table 2 illustrates the XRD results of a structural CuO thin film on the glass substrate. According to Table 2, the low value of the crystallite size was obtained for the (-1 1 0) plane, which led to a maximum value of the dislocation density. Dislocation play an essential role in the plastic deformations of crystalline materials. This prevent the synchronized breakage of bonds between atoms in materials and cause gradual deformation by making the one-by-one breakage of single bonds, and also can cause micro strains that lead to changes in d-spacing and lattice parameters. The smaller value of the dislocation density and micro strains were obtained for the crystallite size 122.6 nm. Starting from the second value of the crystallite size (64.1 nm), the dislocation density decreases with increasing crystallite size, which can indicate the improvement of the crystal film quality.

Figure 5 shows the crystal dislocation (δ), micro strain (ϵ), and crystallite size of CuO film variations in terms of d -spacing. According to the diagram, the grain size decreases linearly with increasing the d -spacing up to the (-1 1 0) plane and then increases. According to Eq. (2), the dislocation density has an inverse relationship with the crystallite size; as a result, the opposite of this situation also occurs for the dislocation density diagram in terms of d -spacing, and the dislocation density increases with the increase in the value of d -spacing. Also, micro strain has an oscillatory relationship with the d -spacing value.

(2) *Field Emission Scanning Electron Microscopy (FESEM)*
The morphology of the prepared nanoparticles was examined using field emission scanning electron microscopy (FESEM). Figure 6 shows the surface morphology of the copper oxide nanoparticles on the glass substrate in a: 1000x, b: 5kx, c: 10Kx, and d: 50Kx magnifications. And the histogram of particle size distribution is shown in Fig. 7. The histogram shows that the maximum size distribution of nanoparticles is in the ranges of 60-80 nm and 80-100 nm. FESEM image describes the morphology of the porous nanoparticles in a variety of shapes and sizes. The nanoparticles on the surface of the glass were deposited almost in a cluster form and have an average size of 80 nm. Compared with their larger counterparts, this nanocluster exhibits attractive electronic, optical,

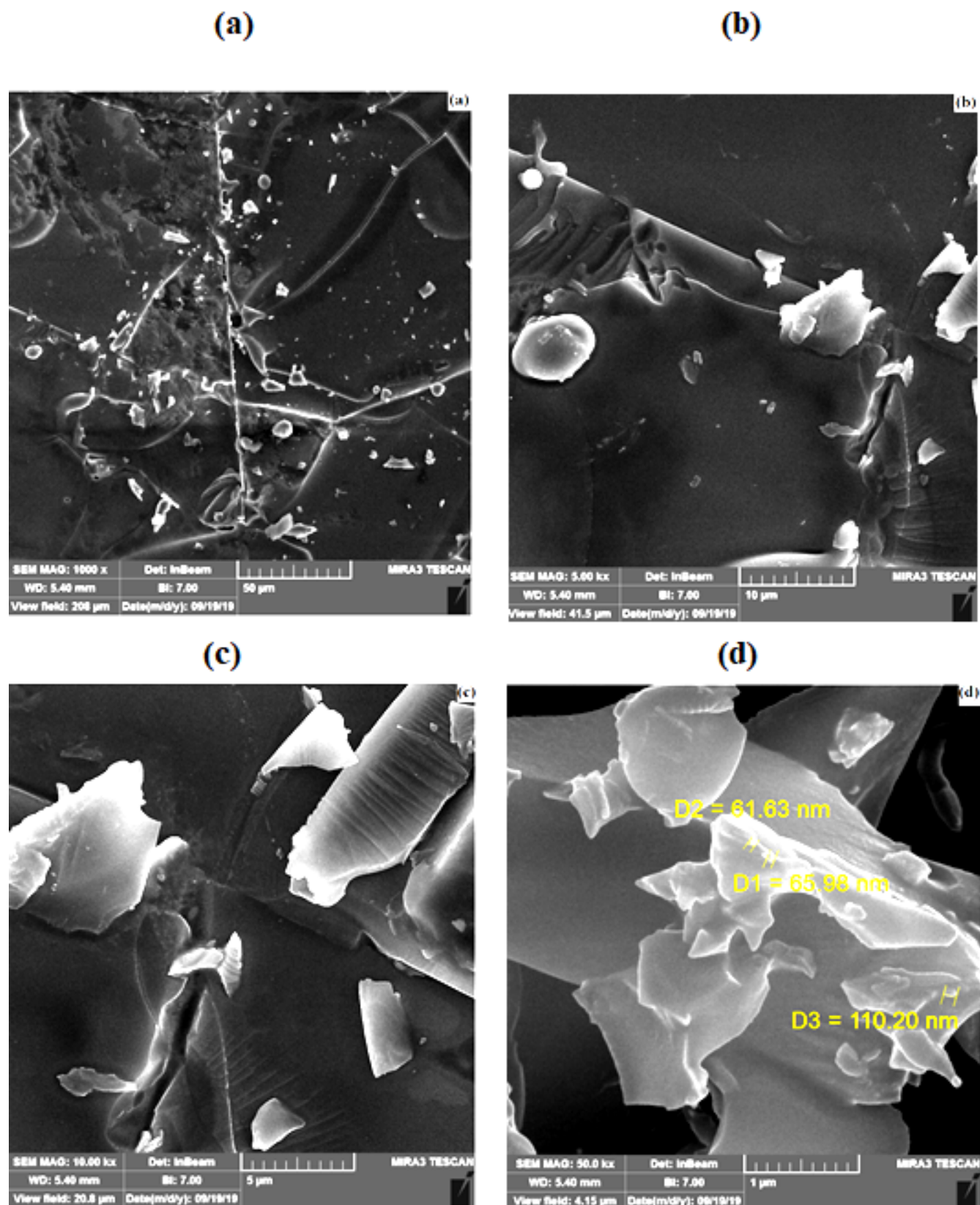


Figure 6. FESEM image of CuO thin film in a) 1000x, b) 5kx, c) 10Kx. d) 50Kx magnifications.

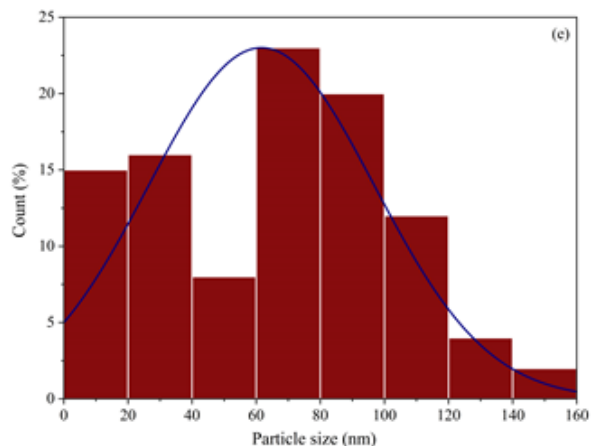


Figure 7. Particle size distribution histogram of CuO thin film on glass substrate.

and chemical properties.

(3) Energy-dispersive X-ray spectroscopy (EDX)

EDX analysis was employed to identify the elements constituting the sample. An electron beam with an energy of 10–20 keV strikes the conducting sample's surface, causing X-rays to emit from the material, and the energy of the emitted X-rays depends on the element of the material under examination. Figure 8 shows the EDX spectrum of the grown elements on the substrate at 25 shots of PF device. The intense peak is due to the Si (substrate) with a weight percentage of 56.84 and other peaks are for oxygen (O) and copper (Cu) with weight percentages of 41.95, and 1.21, respectively. The ratio of Cu and O in EDX analysis is almost 0.028 for the CuO thin film.

(4) Atomic Force Microscopy (AFM)

To measure the roughness of the CuO thin film surface, an atomic force microscope was used in a non-contact state with a sharp needle of about 2 μm and a diameter of less than 10 nm. The AFM image of DPF-coated CuO film on the glass substrate in $1 \times 1 \mu\text{m}$ dimensions shows in Figure 9. AFM measurement shows 125.3 nm as the root means square (RMS) roughness value of CuO film. AFM linear analysis indicates the selected nano-particle size is 17.7 nm, with average thickness of 23.4 nm.

3.2 Optical properties

The optical transmittance spectra of the substrate and CuO thin film recorded in the wavelength range of 200 - 1100 nm are shown in Figure 10. The deposited CuO thin film is found to have very low transmittance at the UV region (200nm–400nm) with an increasing transmittance at the visible region to a high transmittance at the near-infrared region. As seen in Figure 10, the average transmittance of the film on the substrate in the visible area is 83% relatively. The nanoparticle deposition leads to a reduction in transmittance percentage is about 30%.

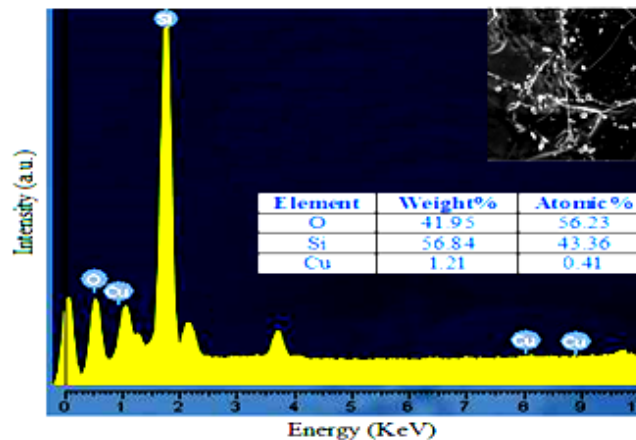


Figure 8. EDX spectra of CuO thin film on glass substrate.

Optical transition in the prepared copper oxide films was characterized by transitions between extended band states. The absorption coefficient α near the absorption edge was determined from the optical transmission measurements at various wavelengths using the Beer-Lambert's law [15,30], given by

$$\alpha = \frac{1}{d} \ln \frac{1}{T} \quad (4)$$

where d is the film thickness, and T is the transmittance. Here, the average film thickness is 1000 nm. Absorption at short wavelengths is due mainly to the interaction of an incoming photon with an electron in an atom. The response of atoms (heavier than electrons) to an electric field results in resonance frequencies much smaller than those of electrons; hence the vibrations of atoms are in the IR, whereas those of electrons lie in the visible and shorter wavelengths [30]. The absorption spectra were used to study the energy band and the type of electronic transitions.

Variation of the absorption coefficient of the film is presented in Fig. 11. As the wavelength increases, the absorption coefficient in the UV region tends to decrease exponentially. This behavior is typical for many semiconductors and could be due to various reasons, such as internal electric fields within the crystal, deformation of lattice due to strain caused by imperfection, and inelastic scattering of charge carriers by phonons [31, 32]. At short wavelengths, photons are often referred to for their energy in electron volts $E(\text{eV}) = hc/\lambda = 1239.8/(\lambda(\text{nm}))$. Using UV-Vis-NIR spectra of deposited film, the bandgap energy (E_g) for CuO film was calculated using Tauc method (Eq.5) [15],

$$(\alpha hv)^2 = A(hv - E_g) \quad (5)$$

where α is the absorption coefficient, hv is the photon energy, A is the constant, and E_g is the bandgap energy. Figure 12 displays the variation of $(\alpha hv)^2$ vs. hv plots for the CuO films. The direct bandgap energy values are obtained by extrapolating the vertical straight line portion of the plot to the

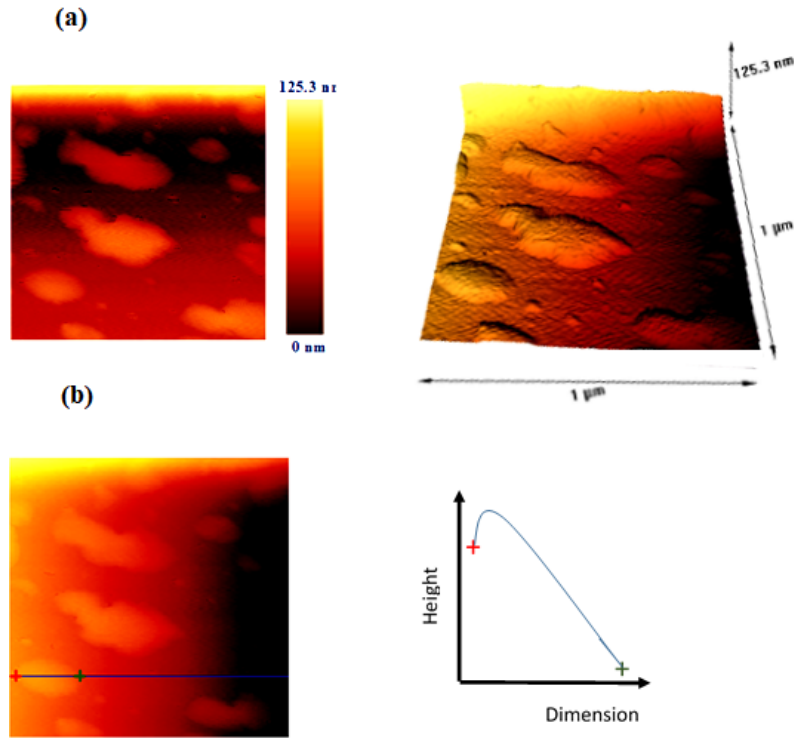


Figure 9. (a) 2 and 3 dimensional AFM images of CuO thin film, and (b) variation of the height of a grain.

photon energy axis (x-axis). The interception on the photon energy axis gives the bandgap energy values as 1.8 eV, which is in good agreement with the results of B. Nada et al. studies [11]. This value is higher than those given in the reference data for bulk CuO [33]. There are several factors influence the bandgap energy of semiconductors. The defects, charged

impurities, disorders at the grain boundaries, as well as the three-dimensional quantum size effects, could increase the energy of the bandgap of nanostructures with the decrease of their size, and discrete energy levels appearing in the band. On the other hand, the particle size of the thin film affects the average transmission of the film, due to the scattering, but does not affect the bandgap energy until the composition is

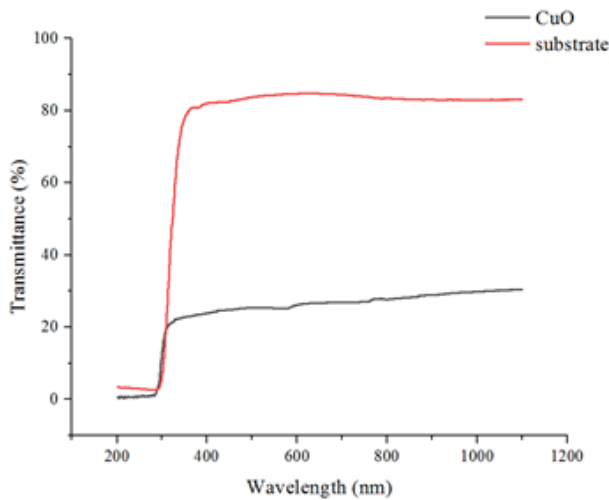


Figure 10. Optical transmittance spectra of the substrate and CuO thin film.

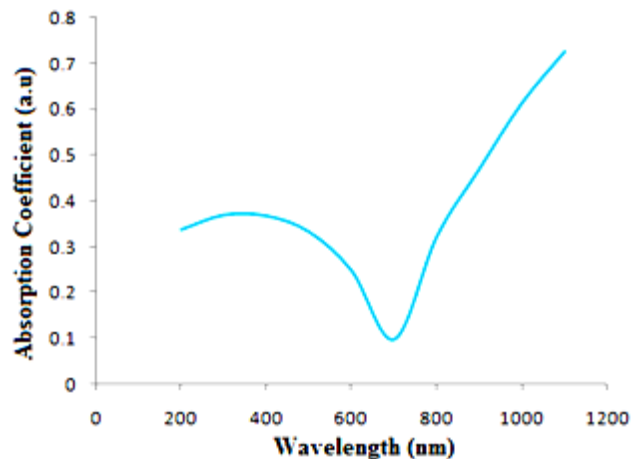


Figure 11. Absorption coefficient spectra of the CuO thin film.

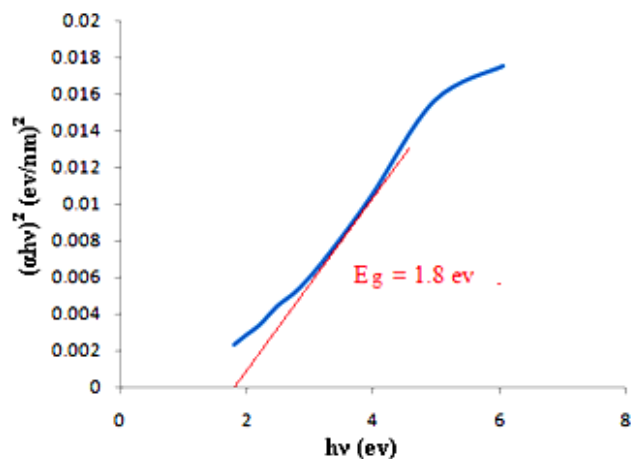


Figure 12. Variation of $(\alpha hv)^2$ vs. hv to extract the bandgap energy of CuO film.

unchanged.

The optical and electronic behavior of semiconductors is decided by two fundamental properties, namely energy gap and refractive index. Generally, the threshold of photon absorption of a semiconductor determines the energy gap, whereas the refractive index is a measure of transparency to the incident photon. Relevance between the bandgap energy and the refractive index was introduced by Herve and Vandamme in the following equation [34],

$$n = \sqrt{1 + \frac{A}{E_g + B}} \quad (6)$$

where A and B are numerical constants that are equal to 13.6 and 3.4 eV, respectively. By substituting values and using equation (6), the refractive index value was calculated to be 1.9, which is smaller than the refractive index value of bulk CuO ($n = 2.6$).

3.3 Electrical properties

A 2 Molar KOH solution was used to measure the I - V characteristics of the substrate and CuO thin film. The current values were measured for different applied voltages from -0.5 to 1.5 V and 20 mV/s rate. Results are shown in Fig. 13.

I - V measurements depends on the applied voltage and electrical conductivity of the CuO film. Studies on the electrical properties of Hall-effect of CuO thin film show that the grown CuO materials are p-type. The p-type conductivity is due to the surplus hole formation in the valence band due to the Cu vacancies in the lattice structure [35]. Compared with cubic Cu_2O , single-phase CuO has high mobility due to low free carrier concentration. The film hole mobility was mainly affected by the content of point defects (i.e., copper vacancies and interstitial oxygen) in the film that determined the free hole concentration. Also, it has a slight optical absorption edge of 1.8 eV. In addition, CuO has high electrical conductivity and thermal stability [36]. The I - V diagram shows that as

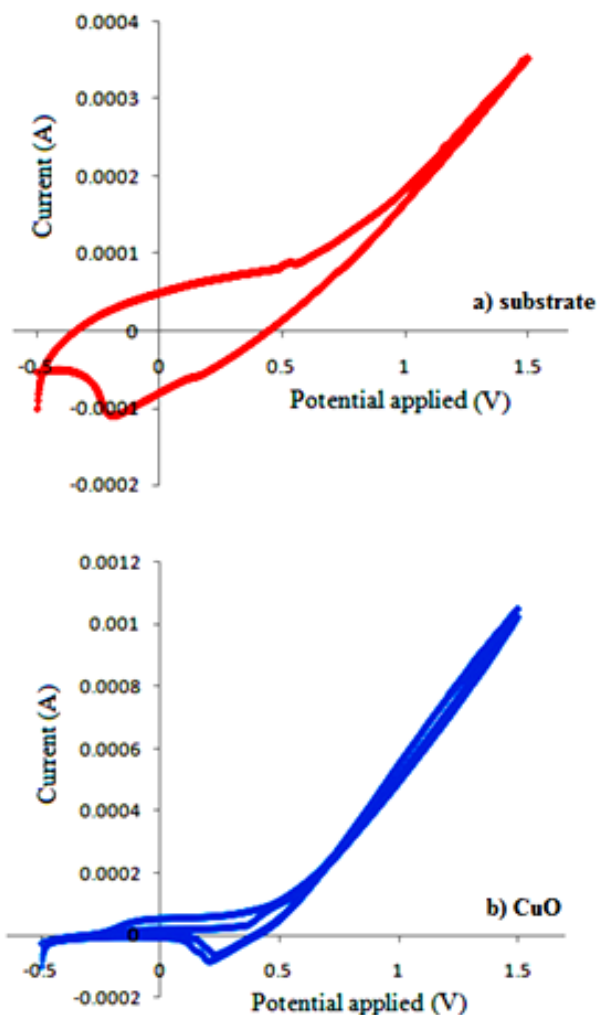


Figure 13. I - V curve of a) substrate, and b) CuO thin film.

the applied voltage increases, the current intensity increases exponentially. It is clear that the I - V characteristic was found to be linear and ohmic irrespective of scan direction without showing any hysteresis effect. The ohmic characteristics are due to the higher number of free carriers than the number of carriers injected into the system. The electrical resistance of metallic thin film is measured by a four-probe method. The sheet resistance was determined by measuring the ratio of the voltage drop (V) from the two inner probes to the applied current (I) measured from the outer probes. The result was multiplied by a geometric correction factor that depends on the probe geometry, $R_s = K(I/V)$ [37]. Where R_s is the sheet resistance and K is the geometric factor, which is 4.53 for a semi-infinite thin sheet. Four probes were placed on the sample at 2 mm distance from each other, and then the device is applied from 0.01 to 0.15 V, and the sample pass current is read in the range of 0 to 0.001 A. The electrical resistances of glass the substrate and CuO film are $1.8 \times 10^3 \Omega\text{cm}$ and $0.68 \times 10^3 \Omega\text{cm}$, respectively. The dc conductivity (σ) for

CuO film was calculated using the given Eq. 7 [37, 38],

$$\sigma = \frac{I}{V} \times \frac{d}{A} \quad (7)$$

where I is the current, V is the applied potential, d is inter-probe distance, and A is the cross-sectional area of the film. The dc conductivity for glass substrate and CuO film are calculated to be 5.03 S/m and 13.2 S/m, respectively.

4. Conclusions

In this experimental research, a low energy plasma focus device was employed to deposit CuO thin film on the glass substrate at room temperature. The optimum pressure for the excellent pinch in the experiment was 0.2 Torr at 8.7 kV. According to the XRD results, the crystallite size of the CuO thin film is between 64 and 122 nm. FESEM images show that the deposited nanoparticles on the glass substrate are almost clustered with an average size of 80 nm. UV-Vis-NIR results indicates that the deposited CuO thin film has very low transmittance at the UV region with an increasing transmittance at the visible region to a high transmittance at the near Infrared region. Using UV-Vis-NIR spectra, the bandgap energy and refraction index of the film was found to be 1.8 eV and 1.9 respectively. The I-V diagram shows that as the applied voltage increases, the current intensity increases exponentially.

Acknowledgements:

The author thanks Dr. Gharehshabani at Sahand University of Technology for using his laboratory .

Conflict of interest statement:

The authors declare that they have no conflict of interest.

References

- [1]
- [2] O. Diachenko, J. K. Jr, O. Dobrozhan, P. Novak, J. Kovc, J. Skrinarirova, and A. Opanasyuk. *Coatings*, **11**:1392, 2021.
- [3] J. Ghijsen, H. L Tjeng, J. V. Elp, H. Eskes, and T. M. Czyzyk. *Physical review B*, **38**:11322, 1998.
- [4] A. Chen, G. Yang, H. Long, F. Li, Y. Li, and P. Lu. *Thin solid Films*, **517**:4277, 2009.
- [5] A. Chen, G. Yang, H. Long, P. Lu, W. Zhang, and H. Wang. *Materials letters*, **91**:319, 2013.
- [6] B. S. Wange, H. C. Hsiao, J. S. Changa, T. K. Lamb, H. K. Wenb, C. S Hungc, J.S. Youngd, and R.B. Huange. *Sensor and Actuators A*, **171**:207, 2011.
- [7] S. Nandy, N. A Banerjee, E. Fortunato, and R.Martins. *Rev. Adv. Sci. Eng.*, **2**:1, 2013.
- [8] P. Pattanasattayavong, S. Thomas, G. Adamopoulos, A. M. McLachlan, and D. T. Anthopoulos. *Appl. Phy. Letter*, **102**:163505, 2013.
- [9] P. Vengatesh, K. Karthik, T.S Shyju, and P. Kuppusami. *Mater. Lett.*, **220**:197, 2018.
- [10] S. Dolai, R. Dey, S. Das, S. Hussain, R. Bhar, and A. K. Pal. *J. Alloy. Compound.*, **724**:456, 2017.
- [11] R. Nayaka, F. A. Ali, B. Nanda, and et. al. *J. Mater. Res. Technol.*, **9**:11045, 2020.
- [12] L. Zhenzhen, T. Keens, Sh. Ruifang, Sh. Yonglong, and et. al. *Journal of Alloys and Compounds*, **695**:3116, 2017.
- [13] S. K. Wanjala, K. W. Njoroge, E.N. Makori, and M. J. Ngaruiya. *Am. J. Condens. Matter Phys.*, **6**:1, 2016.
- [14] H. Anmar Shukor, A. Haider Alhattab, and I. Takano. *J. Vac. Sci. Technol. B*, **38**:012803, 2020.
- [15] H. B. Saad, A. Mejda, D. Samar, and N. T. Kamoun. *Superlattices and Microstructures*, **142**:106508, 2020.
- [16] R. Shabu, A. Moses Ezhil Raj, C. Sanjeeviraja, and C. Ravidhas. *Mater. Res. Bull.*, **68**:1, 2015.
- [17] G. S. Rejith and C. Krishnan. *Mater. letters*, **106**:87, 2013.
- [18] R. Etefagh, E. Azhir, and N. Shahtahmasebi. *Scientia Iranica*, **20**:1055, 2013.
- [19] Ch. Danny, B. K Sang, L. Kecheng, and R. Gordon. *ACS Appl. Energy Mater*, **2**:7750, 2019.
- [20] F. Syed, Ch. David, A. S. James, A. N. Fox, and J. F. David. *Materials and Design*, **193**:108848, 2020.
- [21] A. Sameer and M. A. Makki Hiba. *Journal of Multidisciplinary Engineering Science Studies*, **2**:532, 2016.
- [22] S. Lee, T. Y. Tou, SP. Moo, MA. Eissa, and KH. Kwek AV. Gholap. *Am. J. Phys.*, **56**:62, 1998.
- [23] S. Ahmad, S. Hussain, M. Sadiq, M. Shafiq, A. Waheed, and M. Zakaullah. *Plasma Phys Controlled Fusion*, **48**:745, 2006.
- [24] M. Hassan, A. Qayyum, R. Ahmad, G. Murtaza, and M. Zakaullah. *J Phys D Appl Phys*, **40**:769, 2007.
- [25] R. S. Rawat, P. Lee, T. White, L. Ying, and S. Lee. *Surf Coat Technol*, **138**:159, 2001.
- [26] R. S. Rawat, W. M. Chew, P. Lee, T. White, and S. Lee. *Surf Coat Technol*, **173**:276, 2003.
- [27] R. S. Mohanty, N. K. Neog, B. B. Nayak, B. S. Acharya, P. Lee, T. L. Tan, and R. S. Rawat. *Nucl Instrum Methods Phys Res, Sect B*, **243**:113, 2006.
- [28] M. Balaji, J. Chandrasekaran, and M. Raja. *Mater. Sci. Semicond. Process*, **43**:104, 2016.
- [29] M. Balaji, J. Chandrasekaran, M. Raja, and S. Rajesh. *J. Mater. Sci. Mater. Electron*, **27**:11646, 2016.
- [30] J. I. Larruquert. *Optical Thin Films and Coatings*. Elsevier.
- [31] T. S. Moss, G. J. Burrel, and B. Ellis. *Semiconductor Opto-Electronics*. Butter worths, London, 1st edition, 1973.

- [32] N. Almqvist. *Surf. Sci.*, **355**:221, 1996.
- [33] O.V Diachenko, O. A. Dobrozhan, A. S. Opanasyuk, M. M. Ivashchenko, T. O. Protasova, D. I. Kurbatov, and A. Cerskus. *Superlattices Microstruct.*, **122**:476, 2018.
- [34] P. Herve and L. K. J. Vandamme. *Infrared Physics and Technology*, **35**:609, 1994.
- [35] P. S. Pawar, R. S. Tikke, V. B. Patil, N. B. Mullani, P. P. Waifalkar, K. V. Khot, A. M. Teli, A. D. Sheikh, and T. D. Dongale. *Mater. Sci. Semicond. Process.*, **71**:102, 2017.
- [36] G. Xiaoyong, D. Yongli, and M. Xue. *Solar Energy*, **191**:205, 2019.
- [37] M. Naftaly, S. Das, J. Gallop, K. Pan, F. Alkhalil, D. Kariyapperuma, S. Constant, C. Ramsdale, and L. Hao. *Electronics*, **10**:960, 2021.
- [38] F. M. Smits. *Bell Syst. Tech. J.*, **37**:711, 1958.